Magnetoelectronic and optical properties of a MoS_2 monolayer

Yen-Hung Ho, Yi-Hua Wang, and Hong-Yi Chen*
Department of Physics, National Taiwan Normal University, Taipei 11677, Taiwan
(Received 24 January 2014; revised manuscript received 21 March 2014; published 21 April 2014)

A generalized tight-binding model is utilized to study Landau-level spectra of monolayer molybdenum disulfide. The intrinsic spin-orbit coupling effectively gives rise to multiple splitting of Landau levels. With a close inspection of wave-function characteristics, these levels can be classified into specific groups in terms of their orbital, spin, and valley signatures. In the calculation of magnetoabsorption spectra, the physical origin of the optical selection rules is clearly resolved. In particular, crossings of absorption lines are available and serve as a unique feature of the spin-orbit coupling. Our numerical results clearly demonstrate the magnetic control of spin and valley charge carriers and provide a basis for future experiments.

DOI: 10.1103/PhysRevB.89.155316 PACS number(s): 71.70.Di, 71.15.Ap, 78.20.Ls

I. INTRODUCTION

Molybdenum disulfide (MoS_2) has drawn tremendous attention in recent years since this layered compound has been thinned down to a single trilayer [1–3]. It is a newly discovered platform to explore the two-dimensional (2D) electronic physics. In areas of research interest, it has certain key advantages over graphene in the race for the next generation of semiconductors, such as the existence of a large energy gap and intrinsic spin-orbit coupling (SOC) [4,5]. Such a coupling effectively removes the spin degeneracy and causes these spin-polarized states having quite different behaviors in inequivalent valleys. This also makes MoS_2 a promising material for future spintronics and valleytronics applications. From the theoretical approach, many efforts have been devoted to model the 2D subbands in a zero magnetic field. Most of them are first-principles calculations [6,7] and various tight-binding methods [8–11] which have attempted to fit the results of the former. With regard to Landau-level properties, to date, only a few tight-binding approaches have been made, which are performed within the $\mathbf{k}\cdot\mathbf{p}$ method [12–15]. However, a complete characterization of the Landau levels and a numerical study of magneto-optical properties are still lacking.

In this paper, we utilize a generalized tight-binding model to numerically study the electronic and optical properties of the spin-orbit coupled MoS_2 responding to an applied magnetic field. The atomic hoppings, spin-orbit coupling, and magnetic field are all taken into account without using approximations. Both Landau energies and Landau wave functions can be simultaneously resolved. In particular, wave functions in terms of sublattices provide an intuitive way to define the quantum state of individual Landau levels. Such an explicit level characterization also plays a crucial role in determining the transition rules in magneto-optical spectra. In this study, we show that Landau levels can be classified into specific groups based on their orbital, spin, and valley natures. In optical spectra, the origin of each absorption peak can be identified, where crossings of absorption lines appear as a direct result of the SOC.

II. SUBBANDS IN A ZERO MAGNETIC FIELD

A MoS_2 monolayer is composed of three atomic layers, a single layer of molybdenum atoms sandwiched by two sulfur layers where the molybdenum layer alone forms a 2D triangular lattice. Each Mo atom interacts with six neighboring Mo atoms, as well as six neighboring S atoms (three on the top layer and three on the bottom). The outermost shells of the Mo atom are $4d$ orbitals and those of the S are $3p$ orbitals.

In our tight-binding calculations, three orbitals of the molybdenum atom ($d_{z^2}, d_{xy}, d_{x^2-y^2}$) are taken into account since subbands near the top of the valence bands and the bottom of the conduction bands are predominantly contributed from these three orbitals. The magnetic quantum numbers of these three orbitals are, respectively, $m_l = 0, -2$, and 2. In contrast, subbands from the d_{xz}, d_{yz} orbitals of molybdenum, and the p_x, p_y, p_z orbitals of sulfide, as well as other inner orbitals, are all in the higher-energy regime, so that they hardly affect low-energy subbands.

Without applying an magnetic field, the primitive unit cell contains a single Mo atom. For low-energy subbands, tight-binding wave functions are built up from orbitals of $|m_l = 0\rangle$, $|-2\rangle$, and $|2\rangle$. The Hamiltonian is, therefore, written as

$$H = \begin{pmatrix} H_{0,0} & H_{0,-2} & H_{0,2} \\ H^*_{0,-2} & H_{-2,-2} & H_{-2,2} \\ H^*_{0,2} & H^*_{-2,2} & H_{2,2} \end{pmatrix}, \tag{1}$$

where the matrix elements are

$$\begin{aligned} H_{0,0} &= 2t_0(\cos 2\alpha + 2\cos\alpha\cos\beta) + \epsilon_1, \\ H_{0,-2} &= -2\sqrt{3}t_2 \sin\alpha \sin\beta + 2it_1(\sin 2\alpha + \sin\alpha\cos\beta), \\ H_{0,2} &= 2\sqrt{3}it_1 \cos\alpha \sin\beta + 2t_2(\cos 2\alpha - \cos\alpha\cos\beta), \\ H_{-2,-2} &= 2t_{11}\cos 2\alpha + (t_{11} + 3t_{22})\cos\alpha\cos\beta + \epsilon_2, \\ H_{2,2} &= 2t_{22}\cos 2\alpha + (3t_{11} + t_{22})\cos\alpha\cos\beta + \epsilon_2, \\ H_{-2,2} &= \sqrt{3}(t_{22} - t_{11})\sin\alpha\sin\beta + 4it_{12}\sin\alpha(\cos\alpha - \cos\beta). \end{aligned} \tag{2}$$

*Author to whom correspondence should be addressed: hongyi@ntnu.edu.tw

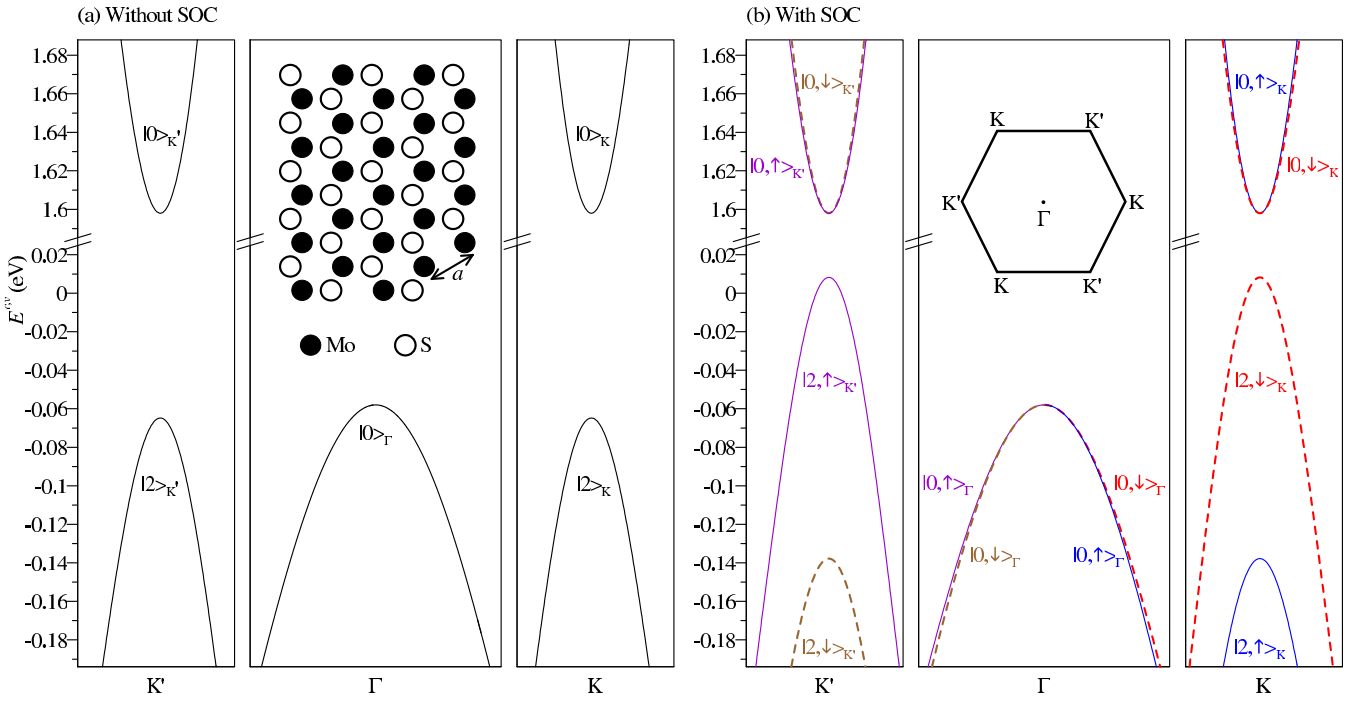

FIG. 1. (Color online) (a) Low-energy bands at $B = 0$ without SOC. Subbands are drawn along k_x, and the band edges are located at highly symmetric points K', Γ, and K. (b) Same plot as (a) but with SOC. The solid blue and purple curves represent the spin-up states in the vicinity of the K and K' valley, respectively, while the dashed red and brown curves shows the spin-down states. The top view of the atomic structure is shown in the inset of (a) and the momentum space in the inset of (b).

Here, $\alpha = \frac{1}{2}k_x a$ and $\beta = \frac{\sqrt{3}}{2}k_y a$. The lattice constant is $a = 3.19$ Å between the neighboring Mo atoms. The hopping parameters between atomic orbitals are chosen as [10] $t_0 = -0.184$ eV, $t_1 = 0.401$ eV, $t_2 = 0.507$ eV, $t_{11} = 0.218$ eV, $t_{22} = 0.057$ eV, and $t_{12} = 0.338$ eV. The on-site energy is $\epsilon_1 = 1.046$ eV added to the $|0\rangle$ orbital and $\epsilon_2 = 2.104$ eV added to the $|-2\rangle$ and $|2\rangle$ orbitals.

With considering the spin degree of freedom, the number of the basis is doubled as $|0, \uparrow\rangle, |-2, \uparrow\rangle, |2, \uparrow\rangle, |0, \downarrow\rangle, |-2, \downarrow\rangle$, and $|2, \downarrow\rangle$. The Hamiltonian related to the intrinsic SOC is given by

$$H' = \lambda \mathbf{L}\cdot\mathbf{S} = \frac{\lambda}{2}\begin{pmatrix} L_z & 0 \\ 0 & -L_z \end{pmatrix}, \tag{3}$$

where

$$L_z = \begin{pmatrix} 0 & 0 & 0 \\ 0 & 0 & 2i \\ 0 & -2i & 0 \end{pmatrix}, \tag{4}$$

and the coupling strength $\lambda = 0.073$ eV. This coupling takes place between the $|-2\rangle$ and $|2\rangle$ orbital electrons with the same spin orientation.

In the absence of a magnetic field, low-energy electronic structures without SOC are shown in Fig. 1(a). They are 2D subbands with band edges located at the highly symmetric points K, Γ, and K' in momentum space. In valence bands, subbands around the Γ point are attributed to the $|0\rangle$ orbital while subbands around the K and K' valleys result from the $|-2\rangle$ and $|2\rangle$ orbitals. In conduction bands, only $|0\rangle$ appears around the K and K' valleys where $|-2\rangle$ and $|2\rangle$ are absent. In addition, the spin-up and spin-down states are fully degenerate. Thus, subbands are symmetric about the Γ point and states around the K and K' valleys are nondistinguishable. The very top of the valence bands is at the Γ point, which is about 6.8 meV higher than those at the K and K' valleys. The system with such a band structure is a semiconductor with an indirect energy gap of 1.655 eV.

These degenerate spin states are effectively split by the intrinsic SOC, as shown in Fig. 1(b). The splitting is particularly evident for valence bands near the K and K' valleys, but it is relatively minor elsewhere. Energetically, spin-up and spin-down subbands are, respectively, shifted up and down by 73 meV ($=\lambda$) for states at the K' valley. This trend is, however, opposite for the K valley states. The splitting of opposite spin states is up to 0.146 eV ($=2\lambda$), which turns the system into a direct-gap semiconductor with the energy gap reduced to 1.59 eV. It is noteworthy that the spin-up and spin-down subbands are interchanged as they are in opposite valleys (K or K'). This means that the intrinsic SOC might enable the manipulation of the combined spin and valley degrees of freedom in such an atomic-thin layer. In our calculations of Landau levels, we found that two spin states from inequivalent valleys respond quite differently to a magnetic field. Furthermore, we numerically study magneto-optical spectra, which practically reveal the multiple splittings of spin, valley, and Landau states.

III. LANDAU-LEVEL STRUCTURES

In the presence of a perpendicular magnetic field $B\hat{z}$ with the vector potential $\vec{A} = (0, Bx, 0)$, a Peierls phase

$\Delta G(\mathbf{R}_\alpha,\mathbf{R}_\beta) = \int_0^1 (\mathbf{R}_\alpha - \mathbf{R}_\beta)\cdot \mathbf{A}[\mathbf{R}_\beta + \lambda(\mathbf{R}_\alpha - \mathbf{R}_\beta)]d\lambda$ is additionally implemented in a tight-binding model [16,17]. The magnetic field needed for a flux quantum ϕ_0 through the lattice cell corresponds to $B_0 = 2.3464 \times 10^4$ T. Thus, the magnetic supercell has to be expanded to $m = B_0/B$ times larger as $\sum_{j=1}^{m}\{|0\rangle^j + |-2\rangle^j + |2\rangle^j\}$ in order to satisfy the periodic boundary condition caused by this magnetic phase [16,17]. The matrix elements of the magnetic Hamiltonian become

$$
\begin{aligned}
H_{0,k;0,j} &= t_0 e^{i2\alpha}\delta_{j,k-2} + 2t_0\cos\beta_j e^{i\alpha}\delta_{j,k-1} + t_0 e^{-i2\alpha}\delta_{j,k+2} + 2t_0\cos\beta_{j-1}e^{-i\alpha}\delta_{j,k+1} + \epsilon_1\delta_{j,k},\\
H_{0,k;-2,j} &= t_1 e^{i2\alpha}\delta_{j,k-2} + [t_1\cos\beta_j + \sqrt{3}it_2\sin\beta_j]e^{i\alpha}\delta_{j,k-1} - t_1 e^{-i2\alpha}\delta_{j,k+2} + [-t_1\cos\beta_{j-1} - \sqrt{3}it_2\sin\beta_{j-1}]e^{-i\alpha}\delta_{j,k+1},\\
H_{0,k;2,j} &= t_2 e^{i2\alpha}\delta_{j,k-2} + [-t_2\cos\beta_j + \sqrt{3}it_1\sin\beta_j]e^{i\alpha}\delta_{j,k-1} + t_2 e^{-i2\alpha}\delta_{j,k+2} + [-t_2\cos\beta_{j-1} + \sqrt{3}it_1\sin\beta_{j-1}]e^{-i\alpha}\delta_{j,k+1},\\
H_{-2,k;-2,j} &= t_{11}e^{i2\alpha}\delta_{j,k-2} + \left[\frac{1}{2}(t_{11}+3t_{22})\cos\beta_j\right]e^{i\alpha}\delta_{j,k-1} + t_{11}e^{-i2\alpha}\delta_{j,k+2} + \left[\frac{1}{2}(t_{11}+3t_{22})\cos\beta_{j-1}\right]e^{-i\alpha}\delta_{j,k+1} + \epsilon_2\delta_{j,k},\\
H_{2,k;2,j} &= t_{22}e^{i2\alpha}\delta_{j,k-2} + \left[\frac{1}{2}(3t_{11}+t_{22})\cos\beta_j\right]e^{i\alpha}\delta_{j,k-1} + t_{22}e^{-i2\alpha}\delta_{j,k+2} + \left[\frac{1}{2}(3t_{11}+t_{22})\cos\beta_{j-1}\right]e^{-i\alpha}\delta_{j,k+1} + \epsilon_2\delta_{j,k},\\
H_{-2,k;2,j} &= t_{12}e^{i2\alpha}\delta_{j,k-2} + \left[-i\frac{\sqrt{3}}{2}(t_{22}-t_{11})\sin\beta_j - 2t_{12}\cos\beta_j\right]e^{i\alpha}\delta_{j,k-1}\\
&\quad - t_{12}e^{-i2\alpha}\delta_{j,k+2} + \left[i\frac{\sqrt{3}}{2}(t_{22}-t_{11})\sin\beta_{j-1} + 2t_{12}\cos\beta_{j-1}\right]e^{-i\alpha}\delta_{j,k+1},
\end{aligned}
\tag{5}
$$

where $\cos\beta_j = \cos[\beta + \pi\frac{\phi}{\phi_0}(j+\frac{1}{2})]$ and $\sin\beta_j = \sin[\beta + \pi\frac{\phi}{\phi_0}(j+\frac{1}{2})]$.

Landau levels in the conduction band without the SOC are shown in Fig. 2(a). The energy as a function of B is illustrated in the left panel. The Landau levels are all close to being linear in B, resulting from the magnetic quantization of parabolic bands at $B = 0$. In our model study, Landau levels can be classified into specific groups. In each group, each level can be further labeled by a Landau index n. The

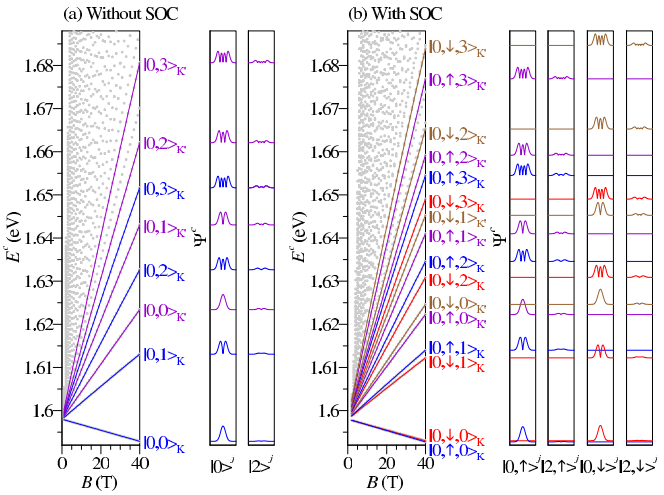

FIG. 2. (Color online) (a) Conduction-band Landau states without SOC: The low-lying Landau levels as a function of B and the Landau wave functions at $B = 40$ T are shown in sublattices, where the K and K' valley states are respectively colored blue and purple. In the wave-function plot, the width of the horizontal axis is 60 nm centered at the middle of the magnetic supercell. (b) Same plot as (a) but with SOC. The K and K' valley states with spin up are colored blue and purple while those with spin down are colored red and brown, respectively.

Landau-level characterization is made according to the way the wave functions distribute in between their sublattices, which will be discussed in detail below.

The right panel shows spatially resolved wave functions. All bases in the magnetic supercell can be divided into sublattices of different orbitals. Without the SOC, these bases are $|0\rangle^j$, $|-2\rangle^j$, and $|2\rangle^j$. Here $|-2\rangle^j$ (not shown) is exactly identical to $|2\rangle^j$ since they have the same magnitude of the magnetic quantum number, i.e., $|m_l| = 2$. In our numerical results, Landau wave functions consist of certain oscillation modes in the sublattices. Since our calculations are performed in Cartesian coordinates, these oscillation modes are close to being Hermite polynomials of a certain order n. For each Landau level, wave functions may have different weights in between sublattices. For instance, conduction-band levels are mainly contributed from the $|0\rangle^j$ sublattice. Thus, the Landau index n is defined as the node number in oscillation of $|0\rangle^j$. In this way, each Landau level can be labeled as $|m_l,n\rangle_\tau$, where m_l, n, and τ are the orbital, Landau, and valley index, respectively.

For conduction states without the SOC, two groups of Landau levels are identified as $|0,n\rangle_K$ and $|0,n\rangle_{K'}$. One comes from states at the K valley and the other from the K' valley. The K group is of a lower energy compared to the K' group. In each group, Landau energies sequentially increase with the increment of n. As B decreases, more Landau levels fall into the low-energy regime. Specifically, all levels shift downward except for the threshold level $|0,0\rangle_K$. After reaching the low-field limit, all low-lying levels are degenerate at 1.598 eV, which exactly corresponds to the bottom of the conduction bands at $B = 0$.

The intrinsic SOC significantly enriches the Landau-level structures, as shown in Fig. 2(b) for conduction states. The spin degeneracy is effectively lifted. Each Landau level is close to the other with the same valley index τ and the same Landau index n but with opposite spin. Except for the two lowest levels, for the K valley states, the spin-up levels are upshifted while

the spin-down levels are downshifted. This trend is, however, opposite for the K' valley states. Such a spin splitting is more evident for levels with the higher Landau index n as well as in a stronger magnetic field. Also, note that the spin splitting in the conduction band is readily apparent in a magnetic field, even though it is still barely observable at $B = 0$.

In terms of wave functions, constituent sublattices are doubled to accommodate the spin degree of freedom, i.e., $|0,\uparrow\rangle^j$, $|-2,\uparrow\rangle^j$, $|2,\uparrow\rangle^j$, $|0,\downarrow\rangle^j$, $|-2,\downarrow\rangle^j$, and $|2,\downarrow\rangle^j$. In between the sublattices, the wave functions of the conduction states are dominated by either the $|0,\uparrow\rangle^j$ or $|0,\downarrow\rangle^j$ sublattices. The Landau index is thus defined as the node number on the $|0,\uparrow\rangle^j$ sublattice for spin-up levels and that on the $|0,\downarrow\rangle^j$ for spin-down levels. Since the wave function is completely contributed from sublattices of either spin directions, each Landau level can be dedicated to a specific spin state. This also implies that the spin flip is strictly prohibited in this spin-orbit coupled system.

Landau levels in valence band appear to be much more complicated, as shown in Fig. 3(a) for the case without the SOC. The green curves illustrate the group condensed from the zero-field subband around the Γ point. The levels of this group are all shifted toward E_F as B decreases, and in the low-field limit, they reach −58 meV. In the view of wave functions, the $|0\rangle^j$ sublattice dominates and its node number is taken to be the Landau index n. Accordingly, the levels in this group are labeled as $|0,n\rangle_\Gamma$.

The rest of the valence Landau levels have a quite different nature since they come from zero-field subbands near the K and K' valley. Those levels can be grouped into K and K' valley states, which are respectively colored blue and purple in Fig. 3(a). The wave functions are dominated by both $|-2\rangle^j$ and $|2\rangle^j$ sublattices. By using the node number to define the Landau index, the Landau levels of the two groups are labeled as $|2,n\rangle_K$ and $|2,n\rangle_{K'}$. Notably, two levels from different valleys are paired together as the Landau index of the K group is two greater than that of the K' group, i.e., levels of $|2,n+2\rangle_K$ and $|2,n\rangle_{K'}$ are close to each other. The first two levels, $|2,0\rangle_K$ and $|2,1\rangle_K$, however, are left unpaired. As B decreases, all levels of both K and K' valley groups move toward E_F, except for the $|2,0\rangle_K$ level. They eventually reach −64.8 meV, which is 6.8 meV lower than that of the Γ valley group.

In valence bands, Landau levels are substantially altered by the intrinsic SOC, as shown in Fig. 3(b). For all three valley groups (Γ, K, and K'), the spin degeneracy is effectively lifted, so that the Landau levels are further divided into groups of $|0,\uparrow,n\rangle_\Gamma$, $|0,\downarrow,n\rangle_\Gamma$, $|2,\uparrow,n\rangle_K$, $|2,\downarrow,n\rangle_K$, $|2,\uparrow,n\rangle_{K'}$, and $|2,\downarrow,n\rangle_{K'}$. The split of opposite spin states is in the 0.1 meV scale for the Γ valley group but up to 146 meV (=2λ) for both K and K' groups. For the K valley group, the spin-up levels are shifted away from E_F by the energy λ while the spin-down levels are moved toward E_F by λ. This trend is, however, opposite for the K' valley group. As a result, groups of opposite valley and opposite spin states are teamed up with each other. One team is the group of $|2,\downarrow,n\rangle_K$ and $|2,\uparrow,n\rangle_{K'}$, where levels reach 8.2 meV as B approaching zero. The other team is the group of $|2,\uparrow,n\rangle_K$ and $|2,\downarrow,n\rangle_{K'}$ that reach −137.8 meV. In addition, for each team, levels are paired if the Landau index n differs by two, i.e., $|2,\downarrow,n+2\rangle_K$ with $|2,\uparrow,n\rangle_{K'}$ and $|2,\uparrow,n+2\rangle_K$ with $|2,\downarrow,n\rangle_{K'}$. In contrast, levels of $|2,\downarrow,0\rangle_K$, $|2,\downarrow,1\rangle_K$, $|2,\uparrow,0\rangle_K$, and $|2,\uparrow,1\rangle_K$ are left unpaired.

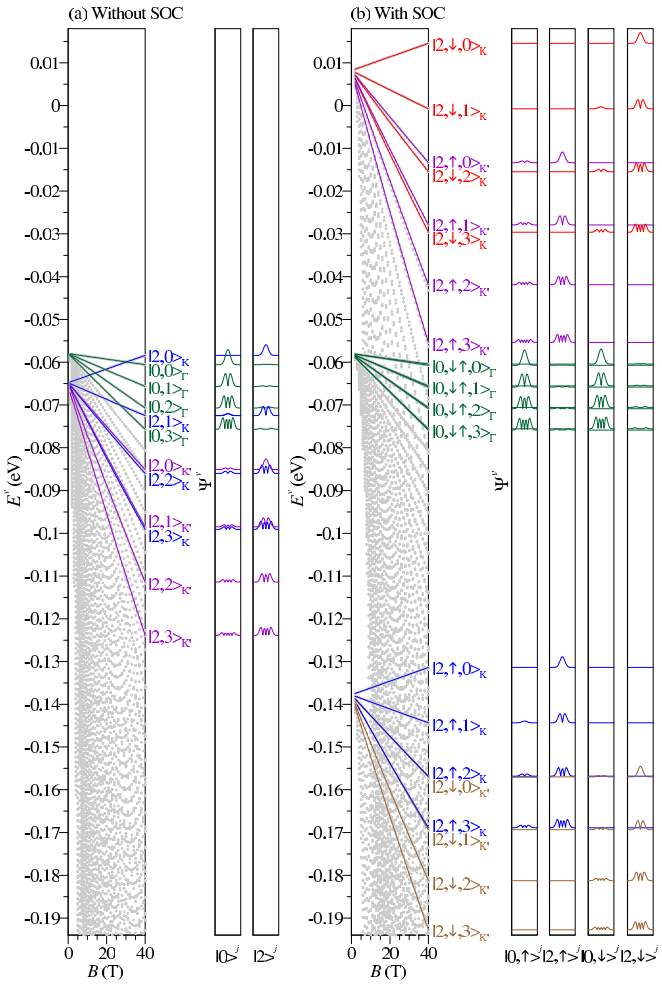

FIG. 3. (Color online) Same plot as Fig. 2 but for the valence-band Landau states. Additionally, the Γ valley states are colored green.

IV. MAGNETO-OPTICAL SPECTRA

In the calculation of optical absorption spectra, the velocity matrix which evaluates the transition rate is calculated using the gradient approximation [18]. For the incident photon with electric polarization parallel to the $\hat{x}$ axis, the velocity matrix elements are the first-order derivative of the original Hamiltonian elements $\langle\Psi^c|\partial H/\partial k_x|\Psi^v\rangle$. In our calculations, most spectral features appear at $k_x = k_y = 0$, where the velocity matrix reads

$$\frac{\partial H}{\partial k_x} = \begin{pmatrix} 0 & i3at_1 & 0 \\ -i3at_1 & 0 & 0 \\ 0 & 0 & 0 \end{pmatrix}, \tag{6}$$

which implies that the most active terms are closely related to the hopping between the $|0\rangle$ and $|-2\rangle$ orbitals of the nearest-neighboring Mo atoms. The optical transition rules also depend on the wave functions of occupied and unoccupied electronic states, Ψ^v and Ψ^c.

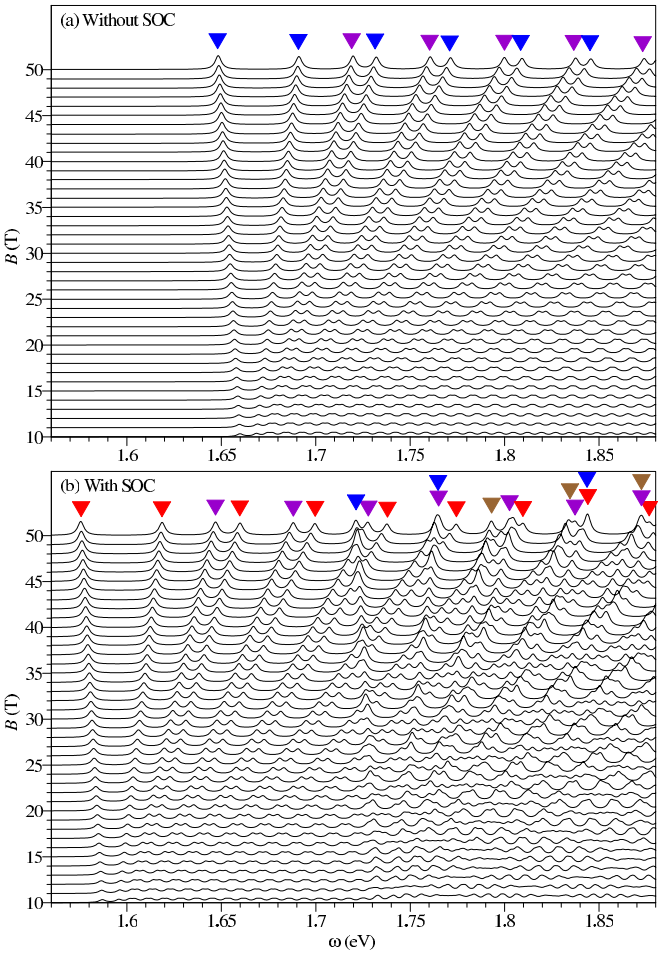

FIG. 4. (Color online) The magneto-optical absorption spectra at different B for the cases (a) without SOC and (b) with SOC. The absorption rates are in arbitrary units and the spectra are offset for clarity. Different types of transitions are distinguished by colored triangles.

The calculated magneto-optical spectra without SOC are shown in Fig. 4(a), where from bottom to top illustrate the field evolution from 10 to 50 T. Absorption peaks are originated from transitions between dispersionless Landau levels. The peak frequencies as a function of B are shown in Fig. 5(a) for a clearer illustration, where the symbol size represents the peak intensity. Absorption peaks are more pronounced in a stronger magnetic field, resulting from the greater Landau quantization. In addition, absorption lines scale linearly in B. They are blueshifted as B increases, except for the threshold one. All absorption peaks can be classified into two types, as marked by blue and purple triangles in Fig. 4(a). The transitions of these two types are

$$\begin{aligned} |2,n\rangle_K &\rightarrow |0,n\rangle_K, \\ |2,n\rangle_{K'} &\rightarrow |0,n\rangle_{K'}. \end{aligned} \tag{7}$$

In each type, the states associated with the first three transitions are also indicated in Fig. 5(a). Also note that most absorption peaks appear in pairs, where each pair consists of transitions of $|2,n\rangle_{K'} \rightarrow |0,n\rangle_{K'}$ and $|2,n+2\rangle_K \rightarrow |0,n+2\rangle_K$.

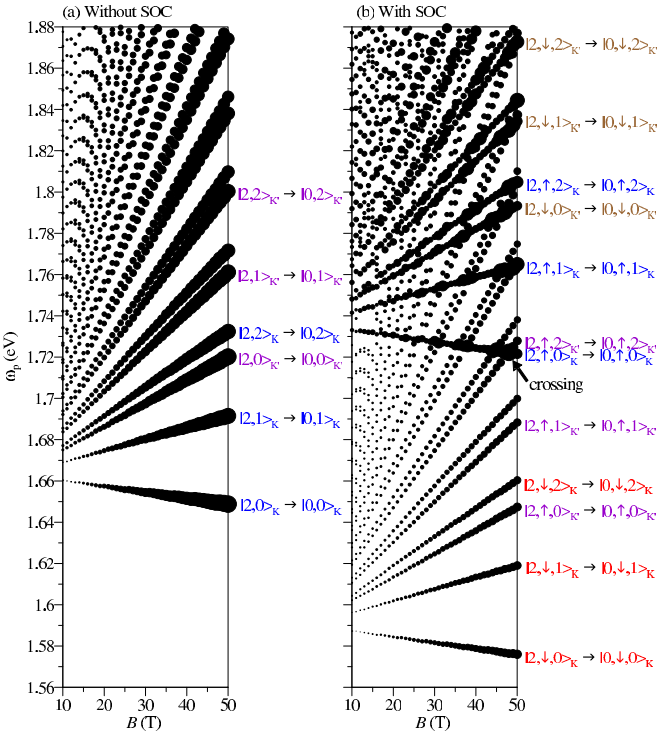

FIG. 5. (Color online) B-dependent absorption frequencies for the cases (a) without SOC and (b) with SOC. The symbol size is proportional to the peak intensity. In each type of transition, states involving the first three absorption lines are also indicated.

As optical transitions occur, the following requirements must be satisfied. First, only transitions between the $|-2\rangle$ and $|0\rangle$ orbital states are available since the related terms in the velocity matrix are nonvanishing, as shown in Eq. (6). Second, two states must belong to the same valley states due to the lack of intervalley scattering. In other words, transitions occur only between two K states and between two K' states. Those involving Γ states are absent in low-lying spectra. Third, the valence and conduction states must be of the same Landau index n. This makes two states having the same oscillation modes in their wave functions. Therefore, by virtue of the orthogonal properties of the Hermite polynomials, the product of the two wave functions in the velocity matrix elements may have a nonzero value.

The intrinsic SOC effectively lifts spin-up and spin-down states, and thus substantially enriches the magneto-optical spectra, as shown in Figs. 4(b) and 5(b). Due to the removal of the spin degeneracy, the spectral intensity is about half as large compared to the case without the SOC. The absorption peaks can be classified into four types:

$$\begin{aligned} |2,\downarrow,n\rangle_K &\rightarrow |0,\downarrow,n\rangle_K, \\ |2,\uparrow,n\rangle_{K'} &\rightarrow |0,\uparrow,n\rangle_{K'}, \\ |2,\uparrow,n\rangle_K &\rightarrow |0,\uparrow,n\rangle_K, \\ |2,\downarrow,n\rangle_{K'} &\rightarrow |0,\downarrow,n\rangle_{K'}. \end{aligned} \tag{8}$$

In Fig. 4(b), peaks are marked by red, purple, blue, and brown triangles. In addition to the transition rules mentioned above, in the presence of the SOC, transitions are allowed only between

states of the same spin. There are no spin flips during optical excitations. In addition, the threshold absorption frequency $|2,\downarrow,0\rangle_K \rightarrow |0,\downarrow,0\rangle_K$ can directly correspond to the system band gap.

It is also important to note that crossings of the absorption lines can be observed at certain field strengths. For example, the degeneracy of the transitions $|2,\uparrow,0\rangle_K \rightarrow |0,\uparrow,0\rangle_K$ and $|2,\uparrow,2\rangle_{K'} \rightarrow |0,\uparrow,2\rangle_{K'}$ is indicated in Fig. 5(b). These crossings occur more frequently in a range of higher frequency and lower field strength. On the contrary, in the case without the SOC, the absorption lines are lined up next to each other, and those crossings are absent. Such crossings of the absorption lines can serve as a fingerprint of the SOC and have the implication of changing the filling factor in the quantum Hall effect. In addition, those crossings might be able to turn into anticrossings as one further considers many-body terms.

V. CONCLUSIONS

In the spin-orbit coupled MoS_2, an external magnetic field gives rise to the multiple splittings of Landau levels. By means of wave functions, states of different orbital, spin, and valley signatures are all clearly resolved and can be distinguished from one another. In magneto-optical spectra, selection rules can be effectively determined as well. Particularly, crossings of absorption lines are found to be a direct evidence of the SOC. All these predictions can provide a guideline for future magneto-optical experiments [19–21].

Note added in the proof. Recently, we became aware of a recent publication [22], which derives an effective Hamiltonian to characterize Landau levels of monolayer transition metal dichalcogenides.

ACKNOWLEDGMENTS

This work was supported by the National Science Council under Grant No. NSC 101-2112-M-003-005-MY3, National Center for Theoretical Science of Taiwan, and partially supported by the Texas Center for Superconductivity and the Robert A. Welch Foundation under Grant No. E-1070.

[1] K. F. Mak, K. He, J. Shan, and T. F. Heinz, Nat. Nanotechnol. **7**, 494 (2012).
[2] K. F. Mak, K. He, C. Lee, G. H. Lee, J. Hone, and T. F. Heinz, Nat. Mater. **12**, 207 (2013).
[3] M. Chhowalla, H. S. Shin, G. Eda, L.-J. Li, K. P. Loh, and H. Zhang, Nat. Chem. **5**, 263 (2013).
[4] H. Ochoa and R. Roldan, Phys. Rev. B **87**, 245421 (2013).
[5] R. Roldan, E. Cappelluti, and F. Guinea, Phys. Rev. B **88**, 054515 (2013).
[6] Z. Y. Zhu, Y. C. Cheng, and U. Schwingenschlogl, Phys. Rev. B **84**, 153402 (2011).
[7] W. Feng, Y. Yao, W. Zhu, J. Zhou, W. Yao, and D. Xiao, Phys. Rev. B **86**, 165108 (2012).
[8] A. Kormanyos, V. Zolyomi, N. D. Drummond, P. Rakyta, G. Burkard, and V. I. Fal'ko, Phys. Rev. B **88**, 045416 (2013).
[9] E. Cappelluti, R. Roldan, J. A. Silva-Guillen, P. Ordejon, and F. Guinea, Phys. Rev. B **88**, 075409 (2013).
[10] G. B. Liu, W. Y. Shan, Y. Yao, W. Yao, and D. Xiao, Phys. Rev. B **88**, 085433 (2013).
[11] F. Zahid, L. Liu, Y. Zhu, J. Wang, and H. Guo, AIP Adv. **3**, 052111 (2013).
[12] X. Li, F. Zhang, and Q. Niu, Phys. Rev. Lett. **110**, 066803 (2013).
[13] H. Rostami, A. G. Moghaddam, and R. Asgari, Phys. Rev. B **88**, 085440 (2013).
[14] T. Cai, S. A. Yang, X. Li, F. Zhang, J. Shi, W. Yao, and Q. Niu, Phys. Rev. B **88**, 115140 (2013).
[15] F. Rose, M. O. Goerbig, and F. Piechon, Phys. Rev. B **88**, 125438 (2013).
[16] C.-P. Chang, C.-L. Lu, F.-L. Shyu, R.-B. Chen, Y.-K. Fang, and M.-F. Lin, Carbon **42**, 2975 (2004); C.-P. Chang, *ibid.* **43**, 1424 (2005); Y.-H. Ho, J.-Y. Wu, Y.-H. Chiu, J. Wang, and M.-F. Lin, Philos. Trans. R. Soc., A **368**, 5445 (2010).
[17] Y.-H. Lai, J.-H. Ho, C.-P. Chang, and M.-F. Lin, Phys. Rev. B **77**, 085426 (2008); Y.-H. Ho, Y.-H. Chiu, D.-H. Lin, C.-P. Chang, and M.-F. Lin, ACS Nano **4**, 1465 (2010).
[18] Y.-H. Ho, J. Wang, Y.-H. Chiu, M.-F. Lin, and W.-P. Su, Phys. Rev. B **83**, 121201 (2011); Y. H. Ho, S. J. Tsai, M. F. Lin, and W. P. Su, *ibid.* **87**, 075417 (2013); Y.-H. Ho, J.-Y. Wu, R.-B. Chen, Y.-H. Chiu, and M.-F. Lin, Appl. Phys. Lett. **97**, 101905 (2010); Y.-H. Ho, *ibid.* **99**, 011914 (2011).
[19] M. Orlita, C. Faugeras, G. Martinez, D. K. Maude, M. L. Sadowski, and M. Potemski, Phys. Rev. Lett. **100**, 136403 (2008); M. Orlita, C. Faugeras, J. M. Schneider, G. Martinez, D. K. Maude, and M. Potemski, *ibid.* **102**, 166401 (2009).
[20] L.-C. Tung, P. Cadden-Zimansky, J. Qi, Z. Jiang, and D. Smirnov, Phys. Rev. B **84**, 153405 (2011).
[21] N. A. Goncharuk, L. Nadvornik, C. Faugeras, M. Orlita, and L. Smrcka, Phys. Rev. B **86**, 155409 (2012).
[22] A. Kormanyos, V. Zolyomi, N. D. Drummond, and G. Burkard, Phys. Rev. X **4**, 011034 (2014).